Fake tilts in differential wavefront sensing

Research Article | Vol. 27, No. 24 / 25 November 2019 / Optics Express 34505

Optics EXPRESS

Fake tilts in differential wavefront sensing

ENRICO MASSA, CARLO PAOLO SASSO,* AND GIOVANNI MANA

INRIM – Istituto Nazionale di Ricerca Metrologica, Str. delle cacce 91, 10135 Torino, Italy
*c.sasso@inrim.it

Abstract: Two-beam interferometry is a tool of high-precision length-metrology, where displacements are measured to within sub-nanometer resolution and accuracy. Differential wavefront sensing – via phase detection by segmented photodiodes – adds the capability of simultaneously measuring the target translation and rotation. This paper gives an analytical model explaining the observation of fake tilts by a combined x-ray and optical interferometer.

1. Introduction

Two-waves laser interferometry is an essential tool in length metrology because of dynamic range, low noise, and traceability to primary realizations of the metre. Displacement measurements with picometer resolution and uncertainty are achievable by using frequency-stabilized laser sources and controlled interferometer operations. Differential wavefront sensing – where the angle between the interfering wavefronts is measured via the phase difference between the travelling fringes detected by segmented photodiodes – makes it possible to simultaneously measure both the target translation and tilts with a single laser beam [1–4]. The working principles, operation, measurement equation, and effect of mismatches and aberrations are reported in [5–7].

This technology is used to align terrestrial gravitational-wave detectors, as VIRGO and LIGO, [8–10] and the Gravity Recovery and Climate Experiment follow-on (GRACE-FO) – a space mission monitoring the Earth gravity field – tests differential wavefront sensing applied to inter-satellite pointing [11]. Also, the Laser Interferometer Space Antenna (LISA) – a foreseen mission designed to detect gravitational waves in space – will use it to monitor the tilt of free-falling masses [3].

The Istituto di Metrologia "G. Colonnetti" (now Istituto Nazionale di Ricerca Metrologica) developed differential sensings in 1993 to cope with Abbe errors in the measurement of the silicon lattice parameter using combined x-ray and optical interferometry [1]. In this experiment, a silicon crystal, which is the movable part of both interferometers, is moved and positioned at successive (integer) optical orders and over displacements up to 5 cm with picometre accuracy and without tilts exceeding 1 nrad [12].

The comparison of simultaneous differential sensing of both the optical and x-ray fringes evidenced disagreements and shear strains in at least one of the gratings (the diffracting planes or optical wavefronts). A cause was traced back to the coupling of transverse displacement and curvature of the optical wavefronts [12,13], but further measurements brought into light additional effects. Obviously, it was impossible to associate the observed strain with certainty to aberrations of the crystal lattice or optical wavefronts. Therefore, additional tests were carried out, which suggested that the problem was the aberration of the optical wavefronts. However, we never investigated mathematically the matter.

Since an imperfect crystal lattice undermines the lattice-parameter measurement, to exclude false observations or guilt assignments, we report a calculation of the phase difference between the travelling fringes produced by aberrated and mismatched beams and detected by a segmented

#371041 https://doi.org/10.1364/OE.27.034505
Journal © 2019 Received 9 Jul 2019; revised 27 Sep 2019; accepted 7 Oct 2019; published 11 Nov 2019

Optics EXPRESS

photo-diode. Contrary to [5–7], which focus on the alignment signals, calibration, and non-linearity, we investigate if the free-of-tilts propagation of slightly mismatched and aberrated – but otherwise parallel – wavefronts originates a differential signal, which is read as a misalignment.

Consistently with our experimental set-up, we assumed the interference pattern much smaller than the detector area and the gaps between the detector elements negligible. In section 2, we summarize the operation of an x-ray/optical interferometer and report about its operation and the observed signals. Next, in section 3, we give first-order models of the propagation of slightly aberrated beams and differential sensing of nearly perfectly aligned wavefronts, e.g., actively controlled it via the feedback of the differential signal. Eventually, we prove that the free-space propagation of mismatched beams and aberrated wavefronts mimic non-existent misalignments.

2. Combined x-ray and optical interferometry

As shown in Fig. 1 (left), a crystal x-ray interferometer consists of three Si blades, 1.2 mm thick, where the {220} planes are orthogonal to the surfaces. X rays (17 keV, Mo K_α line) are split and recombined by multiple Laue diffractions, to obtain coaxial interfering beams of (1×12) mm^2 footprint on the interferometer blades [12].

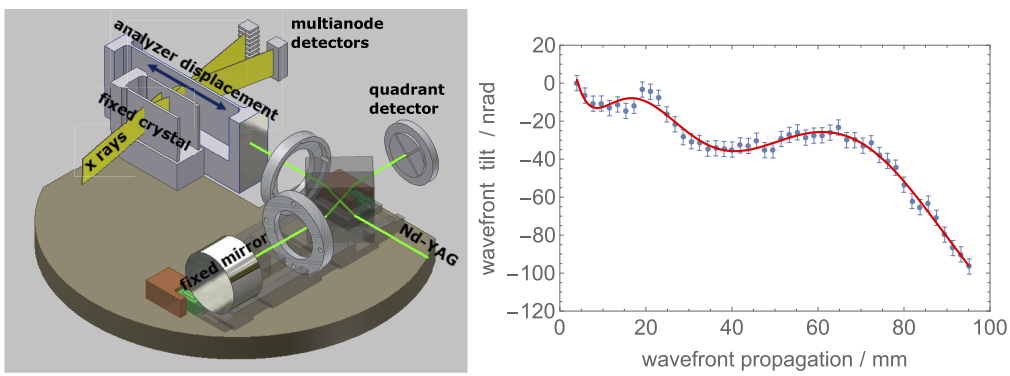

Fig. 1. Left: combined x-ray and optical interferometer. The fixed crystal and optical interferometer rest on a Si plate. Piezoelectric elements under the optics (not shown in the figure) and inertial drivers (red Cu blocks) allow fine alignments to within some tens of μrad. Right: tilt of the laser-beam wavefront inferred by differential wavefront sensing when the analyzer is displaced while keeping the diffracting planes vertical. The red line is a polynomial fit through the measurement data (blue dots). The ±4 nrad error bars correspond to 10% of an x-ray fringe (i.e., about 20 pm) over a 10 mm lever-arm (the analyzer displacement and tilt are half those of the wavefronts).

The analyzer crystal rests on a six degree-of-freedom platform, capable of axial displacements up to 5 cm. The interference signal (having a periodicity equal to the spacing of the diffracting planes, about 0.192 nm) is detected by moving the analyzer orthogonally to the {220} planes (see Fig. 1). The analyzer requires alignment and positioning at the nanoradian and picometre levels. Therefore, its displacement and rotation are measured by optical interferometry; picometre and nanoradian resolutions (in a frequency band up to 10 Hz) are achieved by polarization encoding and phase modulation [14]. Next, positioning at integer fringe orders and alignment are made possible by feedback loops driving piezoelectric elements. To eliminate the adverse influence of the refractive index of air and to ensure millikelvin temperature uniformity and stability, the experiment is carried out in a thermo-vacuum chamber.

The analyzer pitch angle is detected simultaneously by the optical and x-ray interferometers to within nanoradian resolutions.

Optics EXPRESS

The optical measurement of the pitch angle is made (at the integer orders) by fringe detection in the four slices of a quadrant diode. Angles are given by the differential displacements in the vertical and horizontal slice pairs, while the displacement is obtained by averaging the signals. In spite of the limited lever arm, about 1.5 mm, the resolution of the differential measurement is better than 1 nrad.

The x-ray measurement of the pitch angle is made by imaging the interference pattern onto a multianode photomultiplier through a 16 mm pile of eight NaI(Tl) scintillator crystals, with a pixel size of (1×2) mm^2. Owing to the vertical divergence of x-rays, the effective pile height on the analyzer crystal is only 10 mm. Picometer resolution in the subdivision of the x-ray fringes is obtained by the least-squares fit of the interference signals [15]. Therefore, the resolution of the x-ray differential-measurement is better than 1 nrad.

2.1. Measurement procedure

When operating the optical interferometer the interfering beams are set parallel to within 1 μrad by nulling the differential phase readout, the measurement beam is set orthogonal to the analyzer front-mirror to within 10 μrad, the interferometer works with nearly balanced arms (the maximum unbalance is some centimetres), the segment gaps of the photodiode are 10 μm and it is centred with μm resolution [12]. The deviation from flatness of the super-polished analyzer mirror is less than $\lambda/10$ (peak to peak) over 1 cm^2 area; the curvature radius is more than 1 km. The analyzer is moved – up to 5 cm in 1 mm steps – along a straight line, parallel to the laser beam to within 50 μrad uncertainty and with deviations from straightness less than 1 nm. To enhance the stability of the combined interferometer, the fixed crystal and optical set-up rest on a Si plate (see, Fig. 1), without any adjustment devices. Piezoelectric elements placed under the optics and inertial drivers allow fine alignments to within a some tens of microradians.

During each 1 mm step, we drove the analyzer to nullify the phase differences between the x-ray fringes detected by the multianode photomultiplier. In this way, the analyzer keeps its {220} lattice planes parallel to those of the fixed crystal, to within a couple of nano radians. To measure optically the tilt associated to the analyzer displacement and coping with the residual drift between the two interferometers, about 100 nrad/day, we used a modulation technique. Actually, we moved back and forth the analyzer and demodulated the differential signal. Eventually, we accumulated the demodulated results for each 1 mm step to obtain the wavefront tilts over the full 50 mm displacement.

Figure 1 (right) shows that the tilt of the optical wavefronts due to the analyzer displacement, inferred from the demodulated signal of the quadrant photodiode, is not null, as it should have been. The tilt gradient – typically, ±1 nrad/mm – discloses a shear strain of the {220} planes and/or optical wavefronts. But, the data do not allow us to uniquely separate them. Also, we note that the crystal-lattice displacement and shear-strain are half those of the optical wavefronts. The differential signal appeared to depend on the optical interferometer configuration, but not on the x-ray one. On this basis, we excluded crystal strains.

If the laser beam is not orthogonal to the analyzer mirror, the analyzer displacement causes a lateral shift of the measurement beam, and the interferometer senses the wavefront deviations from flatness, smoothed by about 1 mm^2 integration area. In particular, the wavefront curvature originates a differential signal and a seemingly parasitic wavefront-tilt [13]. Also, the beam displacement over the insensitive gap between the photodiode segments, 10 μm, might affect the differential signal. Eventually, a differential signal might originate from the coupling of the lateral shift of the analyzer (due to a displacement non-coaxial to the laser beam) to the roughness of its front mirror, smoothed again by the 1 mm^2 integration area.

The disagreement between the x- and optical-measurement of the wavefront tilt did not evidence dependences on the photodiode alignment nor the same randomness of the orthogonal alignment (to within 10 μrad) of the laser beam and coaxial (to within 50 μrad) movement of the

Optics EXPRESS

analyzer. Therefore, in the next sections, we focus on more subtle effects due to aberrations of the optical wavefronts.

3. Differential wavefront sensing

A free-of-tilts propagation of mismatched and aberrated wavefronts might originate a differential signal. To investigate this problem, and to exclude or quantify it, this section gives a propagation model and the measurement equation of the wavefront tilt.

3.1. Hermite-Gauss modes

Following [2], to describe slightly contaminated, but otherwise identical and coaxial, TEM_{00} interfering beams, it is convenient to introduce an orthogonal set of modes that can be used to expand the optical fields.

The Hermite-Gauss beams,

$$u_{lm}(\xi_1, \xi_2; \zeta) = u_l(\xi_1; \zeta) u_m(\xi_2; \zeta), \tag{1}$$

form a complete orthogonal base for the separable solutions of the paraxial approximation of the scalar wave equation [16]. Since u_{00} – the fundamental TEM_{00} mode – is an ideal diffraction-limited Gaussian beam, their amplitudes are a natural description of the interfering beams.

Omitting the plane wave $\mathrm{e}^{-\mathrm{i}kz+\mathrm{i}\omega t}$ term (where $k = \omega/c$ is the wave-number, ω is the angular frequency, z is the propagation distance, and t is time) the (not normalized) base functions are [17]

$$u_n(\xi; \zeta) = \mathrm{H}_n\left(\frac{\sqrt{2}\xi}{|q|}\right) \frac{|q|^n}{q^n} \frac{\mathrm{e}^{-\mathrm{i}\xi^2/q}}{\sqrt{-\mathrm{i}q}}, \tag{2}$$

where $\mathrm{H}_n(.)$ is the Hermite polynomial of degree n. Also, $q = \mathrm{i} + \zeta$ is the complex propagation parameter and we used the dimensionless coordinates $\xi_{1,2} = x_{1,2}/w_0$ and $\zeta = z/z_R$, where $x_{1,2}$ are the transverse coordinates, w_0 is the $1/\mathrm{e}^2$ radius of the u_0 waist (which occurs at $\zeta = 0$), and $z_R = kw_0^2/2$ is the Rayleigh distance.

3.2. Interferometer operation

To model the two-beam interference, we consider slightly contaminated, but otherwise identical and coaxial, TEM_{00} beams. Next, the measurement beam ψ_m (which travels through the variable arm) is propagated (with respect the ψ_r reference) by a distance s along its axis.

Hence, by using the scalar and paraxial approximations, we describe each factor of the (separable) interfering fields by the complex amplitudes

$$\psi_{\mathrm{r,m}}(\xi; \zeta) = u_0(\xi; \zeta)\mathrm{e}^{S_{\mathrm{r,m}}(\xi;\zeta)} \approx \frac{\mathrm{e}^{-\mathrm{i}\xi^2/q}}{\sqrt{-\mathrm{i}q}}\left[1 + S_{\mathrm{r,m}}(\xi; \zeta)\right], \tag{3}$$

where u_0 is the TEM_{00} ξ-component and the real and imaginary parts of $S_{\mathrm{r,m}}(\xi)$ describe small, zero mean, amplitude and wavefront errors. We set $\zeta = 0$ at the detector plane, restricted to a single (either ξ_1 or ξ_2) transverse dimension, and, taking advantage of the $S_{\mathrm{r,m}}$ smallness and limiting the investigation to the leading terms, expanded $\exp(S_{\mathrm{r,m}})$ in series up to the first order.

A way to express $S_{\mathrm{r,m}}(\xi, \zeta = 0)$ is by series expansions in terms of Hermite polynomials. Hence,

$$S_\mathrm{r}(\xi; 0) = -(\xi_0 + \mathrm{i}a)\mathrm{H}_1(\sqrt{2}\xi) - (\mathrm{i}\kappa_\mathrm{r}/8 + \eta)\mathrm{H}_2 + \mathrm{i}\gamma_\mathrm{r}\mathrm{H}_3(\sqrt{2}\xi), \tag{4}$$

$$S_\mathrm{m}(\xi; 0) = \xi_0\mathrm{H}_1(\sqrt{2}\xi) + \eta\mathrm{H}_2(\sqrt{2}\xi) + \mathrm{i}\gamma_\mathrm{m}\mathrm{H}_3(\sqrt{2}\xi), \tag{5}$$

where ξ_0, $\mathrm{i}a$, $\mathrm{i}\kappa_\mathrm{r}$, η, and $\mathrm{i}\gamma_{\mathrm{r,m}}$ are small parameters describing the offset, misalignment, wavefront curvature, radius difference, and wavefront undulation, respectively, of the interfering beams.

Optics EXPRESS

The real coefficients describe aberrations of the intensity profile; the imaginary ones, wavefront aberrations [2,18]. The null imaginary part of the H_1 coefficient in Eq. (5) ensures that ψ_m propagates parallel to its axis. We stopped the $S_{r,m}(\xi, \zeta = 0)$ expansions at H_3 because this is the lowest-order term changing the Gaussian nature of the interfering beams.

In Eq. (3), the u_0 axis, waist, and waist location are arbitrary. We set the z axis collinear to the ψ_m axis and crossing the $\zeta = 0$ plane midway between the beam axes. Also, we located the u_0 waist at $\zeta = 0$ and set its radius as

$$w_0^2 = \frac{2w_r^2 w_m^2}{w_r^2 + w_m^2}, \tag{6}$$

where $w_{r,m} \approx (1 \pm \eta/4)w_0$ are the $\zeta = 0$ radii of $\psi_{r,m}$ and η accounts for their difference. In Eqs. (4) and (5) a, κ_r, and $\gamma_{r,m}$ are expressed in radians, $2\sqrt{2}a = kw_0\alpha$ takes the tilt α of the reference wavefront into account, $\pm x_0 = \pm\sqrt{2}\xi_0 w_0$ are the offsets of the beam axes, $\kappa_r = z_R/R_r$ is the dimensionless curvature of the ψ_r wavefront that adds on the curvature of u_0, and γ_r and γ_m take the H_3 contaminations to the ψ_r and ψ_m wavefronts into account. The small difference between the $\psi_{r,m}(\xi; 0)$ radius implies that the initial unbalance of the interferometer is significantly smaller than z_R. Eventually, we took the initial curvature of the ψ_m wavefront as null; therefore, the ψ_m waist is at $\zeta = 0$.

Expanding $S_{r,m}(\xi, 0)$ in terms of Hermite polynomials corresponds to represent $\psi_{r,m}$ in terms of Hermite-Gauss modes. Hence, by using Eq. (2) and propagating ψ_m by $\varsigma = s/z_R$, the $\zeta = 0$ interfering fields are

$$\psi_r(\xi; 0) = e^{-\xi^2}\left[1 + (a - i\xi_0)u_1(\xi, 0) + (\eta + i\kappa_r/8)u_2(\xi, 0) + \gamma_r u_3(\xi, 0)\right], \tag{7}$$

$$\psi_m(\xi; \varsigma) = e^{-\xi^2}\left[1 + i\xi_0 u_1(\xi, \varsigma) - \eta u_2(\xi, \varsigma) + \gamma_m u_3(\xi, \varsigma)\right]. \tag{8}$$

It is worth noting that the u_1 and u_2 contaminations describe Gaussian beams expressed in an Hermite-Gauss base whose TEM_{00} mode is different from the beams at hand. Only the u_3 contamination inherently changes the nature of ψ_r and ψ_m.

The interference signals, integrated over a segmented detector, are

$$I_\pm(\varsigma) = \int_{a_\pm}^{b_\pm} |\psi_r(\xi; 0) + \psi_m(\xi; \varsigma)|^2 \, d\xi, \tag{9}$$

where the $\pm$ subscripts indicate the lower ($a_- = -\infty$ and $b_- = 0$) and upper ($a_+ = 0$ and $b_+ = +\infty$) areas and we considered one dimension only. The differential phase is

$$\Delta\phi(\varsigma) = \arg(\Xi_+) - \arg(\Xi_-) = \arg(Q) \approx \mathrm{Im}(Q), \tag{10}$$

where $Q = \Xi_+/\Xi_-$,

$$\Xi_\pm(\varsigma) = \int_{a_\pm}^{b_\pm} \psi_r^*(\xi; 0)\psi_m(\xi; \varsigma) \, d\xi, \tag{11}$$

the star is the complex conjugation, $|Q - 1| \ll 1$, and we limited ourselves to the first-order terms.

Optics EXPRESS

Next, by using Eq. (3) in Eq. (11) and expanding Ξ_+/Ξ_- up to the first order of $S_{\mathrm{r,m}}$ via the approximation $(1+B_+)/(1+B_-) \approx 1 + B_+ - B_-$, we obtain

$$Q \approx 1 + \frac{2}{\sqrt{\pi}} \int_0^\infty \mathbb{w}(q) \left[S_{\mathrm{r}}^*(\xi;0) + S_{\mathrm{m}}(\xi;\varsigma) \right] \mathrm{d}\xi - \frac{2}{\sqrt{\pi}} \int_{-\infty}^0 \mathbb{w}(q) \left[S_{\mathrm{r}}^*(\xi;0) + S_{\mathrm{m}}(\xi;\varsigma) \right] \mathrm{d}\xi \quad (12)$$

where the reference and measurement wavefronts are weighed by

$$\mathbb{w}(q) = \sqrt{\frac{\mathrm{i}+q}{q}} \mathrm{e}^{-(\mathrm{i}+q)\xi^2/q} = \sqrt{\frac{2\mathrm{i}+\varsigma}{\mathrm{i}+\varsigma}} \mathrm{e}^{-2\xi^2/\overline{\upsilon}^2} \mathrm{e}^{-\mathrm{i}\kappa_{\mathrm{m}}\xi^2}, \quad (13)$$

$\kappa_{\mathrm{m}} = \varsigma/(1+\varsigma^2)$ is the dimensionless curvature of the $u_0(\xi;\varsigma)$ and $\psi_{\mathrm{m}}(\xi;\varsigma)$ wavefronts, and

$$\overline{\upsilon}^2 = \frac{2(1+\varsigma^2)}{2+\varsigma^2} \quad (14)$$

is the harmonic mean of the (dimensionless) u_0 squared-radii evaluated at $\zeta = 0$ and $\zeta = \varsigma$, which are equal to 1 and $1+\varsigma^2$. The square root indicates the principal value, and the imaginary part of the complex square root has a branch cut along the negative real axis.

By carrying out the integrations in Eq. (12), where $S_{\mathrm{r,m}}(\xi)$ are made explicit by comparing Eq. (3) to Eqs. (7) and (8), we obtain an expression for the differential phase that turns out to be a linear combination of terms proportional to the coefficients introduced in Eqs. (4) and (5) [19]

$$\begin{aligned} \Delta\phi(\varsigma) &= 4\sqrt{2/\pi}\,\mathrm{Im}\left(\sqrt{\frac{q}{\mathrm{i}+q}}A_1\right) + 32\sqrt{2/\pi}\,\mathrm{Im}\left(\sqrt{\frac{q^3}{(\mathrm{i}+q)^3}}A_3\right) \\ &= c_\alpha a + c_0\xi_0 + c_{\mathrm{r}}\gamma_{\mathrm{r}} + c_{\mathrm{m}}\gamma_{\mathrm{m}}, \end{aligned} \quad (15)$$

where

$$A_1 = \mathrm{i}a + \frac{\mathrm{i}-q}{q}\xi_0 + 6\mathrm{i}\gamma_{\mathrm{r}} - \frac{6|q|^2}{q^3}\gamma_{\mathrm{m}}, \quad (16)$$

$$A_3 = \frac{1}{q^3}\gamma_{\mathrm{m}} - \mathrm{i}\gamma_{\mathrm{r}}, \quad (17)$$

and the c_α, c_0, c_{r}, c_{m} coefficients will be made explicit in the following sections. In addition to the tilt, $\Delta\phi(\varsigma)$ depends on the beam-axis offset and TEM_{30} contaminations, but not on the wavefront curvature and beam-radius difference. In fact, at the first-order approximation, the radius and wavefront curvature differences only describe a Gaussian beam having waist radius and location different from those of u_0 and, therefore, traceable to the freedom of the u_0 choice.

3.3. Measurement equation

Differential sensing delivers information on the wavefront misalignment in a way similar to a sine bar [1]. Hence, to determine the measurement equation, we set the $\xi_0 = \gamma_{\mathrm{r,m}} = 0$ and consider the interference of two tilted Gaussian beams. From Eq. (15), the result is

$$\Delta\phi(\varsigma) = c_\alpha a = 4\sqrt{\frac{2}{\pi}}\mathrm{Re}\left[\sqrt{\frac{q}{\mathrm{i}+q}}\right] a, \quad (18)$$

where $2\sqrt{2}a = kw_0\alpha$ and α is the misalignment. The differential phase is shown in Fig. 2 (left) together with the

$$\Delta\phi(\varsigma) \approx \frac{4\overline{\upsilon}a}{\sqrt{\pi}} = \frac{2k\overline{w}\alpha}{\sqrt{2\pi}} \quad (19)$$

approximation, where $1 \le \overline{\upsilon}(\varsigma) < \sqrt{2}$ and $\overline{w}(\varsigma) = \overline{\upsilon}w_0$ take the effective radius of the interference pattern after the ψ_{m} propagation into account.

Optics EXPRESS

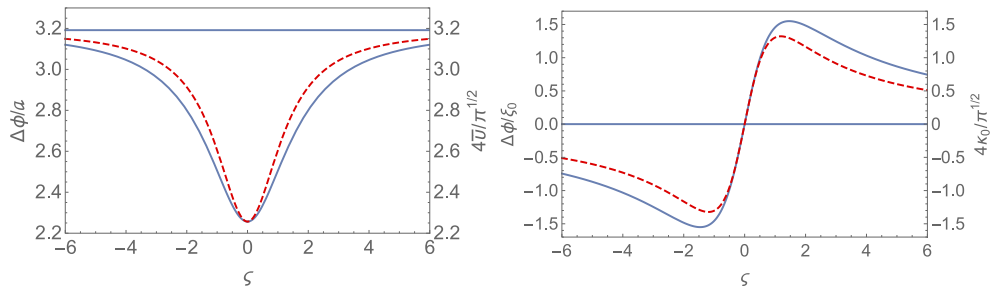

Fig. 2. Left: Differential phase Eq. (18) expected when the reference wavefront is tilted by $2\sqrt{2}a/(kw_0)$ (solid line). The dashed line is the approximation Eq. (19). Right: differential phase Eq. (20) expected when the offset between the axes of the interfering beams is $2\sqrt{2}\xi_0$ (solid line). The dashed line is the approximation Eq. (21). The horizontal lines are the asymptotes for the far-field propagation of the measurement beam.

The calibration factor in Eqs. (18) and (19) depends on the propagation distance. Therefore, as the beam propagates and unless $\alpha = 0$, the gradient of the ψ_{m} radius makes a non-existent misalignment to appear. As Fig. 2 (left) shows, near- and far-field detections are not affected by this problem. Equations (18) and (19) generalize the results given in [13].

4. Aberrated beams

Equation (18) relates the wavefront misalignment to the differential phase at fixed propagation distances. In the presence of aberrations, Eq. (15) includes propagation-dependent offsets that will be now investigated.

4.1. Axis offsets

The axis separation is the only mismatch offsetting the differential phase. From Eq. (15), a $2x_0 = 2\sqrt{2}w_0\xi_0$ separation offsets it by

$$\Delta\phi(\varsigma) = c_0\xi_0 = 4\sqrt{\frac{2}{\pi}}\mathrm{Im}\left[\frac{\mathrm{i} - q}{\sqrt{(\mathrm{i} + q)q}}\right]\xi_0, \tag{20}$$

which is shown in Fig. 2 (right) together with the

$$\Delta\phi(\varsigma) \approx 4\kappa_{\mathrm{m}}\xi_0/\sqrt{\pi}, \tag{21}$$

approximation, where $\kappa_{\mathrm{m}}(\varsigma) = \varsigma/(1 + \varsigma^2)$. Because of the κ_{m} gradient, Eqs. (20) and (21) mimic a parasitic tilt associated with the ψ_{m} propagation.

To explain and check heuristically Eq. (20), we consider the interference of two spherical wavefronts, $k(x \pm x_0)/(2R_{\mathrm{r,m}})$, having radii $R_{\mathrm{r,m}}$ and spaced by $2x_0$. By linearization of their phase difference $\phi(\xi)$ in their $x/w_0 = 0$ intersection point, we obtain

$$\phi(\xi) = \frac{k(\kappa_{\mathrm{r}} + \kappa_{\mathrm{m}})x_0 x}{z_R} = 4\sqrt{2}\,\overline{\kappa}\xi_0\xi, \tag{22}$$

where $\overline{\kappa} = (\kappa_{\mathrm{r}} + \kappa_{\mathrm{m}})/2$ is the mean (dimensionless) curvature, $\kappa_{\mathrm{r,m}} = z_R/R_{\mathrm{r,m}}$, $x = w_0\xi$, $x_0 = \sqrt{2}w_0\xi_0$, and $kw_0^2 = 2z_R$. After equating Eq. (22) to the phase difference $k\alpha w_0\xi$ of two

Optics EXPRESS

plane wavefronts, where α is the tilt inferred from the differential sensing of $\phi(\xi)$,

$$kw_0\alpha = 4\sqrt{2}\,\overline{\kappa}\xi_0 \tag{23}$$

follows. Contrary, by equaling Eq. (19) and Eq. (21), we obtain

$$k\overline{w}\alpha = 2\sqrt{2}\,\kappa_{\mathrm{m}}\xi_0, \tag{24}$$

where α is the tilt inferred from Eq. (21). In Eq. (24), $\overline{w}^2$ – the harmonic mean of w_{r}^2 and w_{m}^2 – takes the increase of the lever arm into account, which increase is not considered in Eq. (23).

The difference between Eqs. (23) and (24) is due to having neglected the second order term $\kappa_{\mathrm{r}}\xi_0$ in Eq. (21), which term accounts for the curvature of the reference wavefront. To take this curvature into account, though this does not affect the $\partial_\xi\Delta\phi$ derivative of our interest, we can upgrade Eq. (21) by empirically substituting $\kappa_{\mathrm{m}} + \kappa_{\mathrm{r}}$ for κ_{m}. With this upgrade, the near-field value of the differential-phase offset is

$$\lim_{\varsigma\to 0}\Delta\phi = 4(\varsigma + \kappa_{\mathrm{r}})\xi_0/\sqrt{\pi}, \tag{25}$$

where we used $\kappa_{\mathrm{m}} = \varsigma/(1+\varsigma^2) \approx \varsigma$.

4.2. TEM_{30} contaminations

The TEM_{30} contamination changes the Gaussian nature of the interfering beam. By setting $\alpha = \kappa_{\mathrm{m}} = 0$ in Eq. (15), we find that it offsets the differential phase by

$$\Delta\phi(\varsigma) = c_{\mathrm{r}}\gamma_{\mathrm{r}} + c_{\mathrm{m}}\gamma_{\mathrm{m}} = 8\sqrt{\frac{2}{\pi}}\mathrm{Im}\left[\frac{\mathrm{i}(q-3\mathrm{i})q^{1/2}}{(\mathrm{i}+q)^{3/2}}\right]\gamma_{\mathrm{r}} + 8\sqrt{\frac{2}{\pi}}\mathrm{Im}\left[\frac{[4q-3(\mathrm{i}+q)|q|^2]}{q^{5/2}(\mathrm{i}+q)^{3/2}}\right]\gamma_{\mathrm{m}}, \tag{26}$$

whose two contributions are shown in Fig. 3. To check the analytical derivation, we examine the meaningfulness of the near- and far-field limits. In the near-field case, the

$$\Delta\phi|_{\varsigma=0} = \frac{8(\gamma_{\mathrm{r}} - \gamma_{\mathrm{m}})}{\sqrt{\pi}} \tag{27}$$

offset is duly proportional to the difference of the wavefront gradients at the beam axes. Also, Fig. 4 shows that, as ψ_{m} propagates, its the weighed wavefront aberration reverses. Eventually, it flattens, while the weighed wavefront error of ψ_{r} inflates. As Fig. 4 suggests,

$$\lim_{\varsigma\to\pm\infty}\Delta\phi = -\frac{8\sqrt{2}\gamma_{\mathrm{r}}}{\sqrt{\pi}}, \tag{28}$$

depends only on the ψ_{r} wavefront.

4.3. Wavefront ripples

By comparing the laser-beam wavefront against the diffracting planes, our x-ray/optical interferometer highlighted $\lambda/10$ (peak-to-valley) errors having a periodicity equal to about the beam radius [20,21]. These observation suggests that the interfering beams might be contaminated by high-frequency modes, e.g., due to the imprinting of imperfections by the surfaces hit or crossed in the beam ways through the interferometer.

Optics EXPRESS

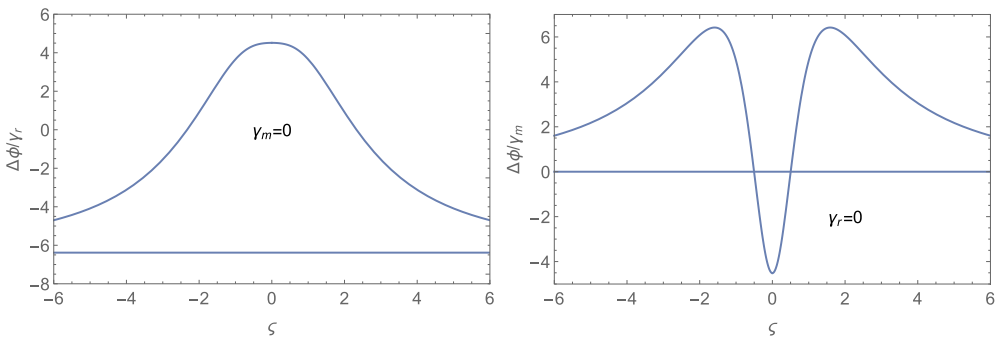

Fig. 3. H_3 contributions – reference (left) and measurement (right) beams – to $\Delta\phi$, see Eq. (26). The horizontal lines are the asymptotes for the far-field propagation of the measurement beam.

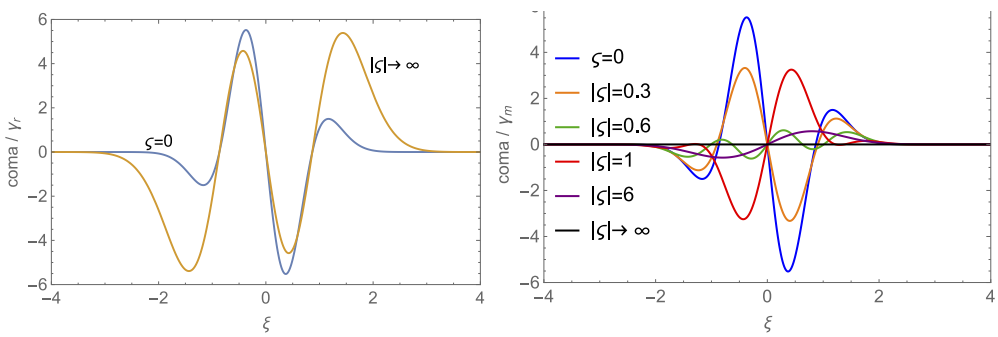

Fig. 4. Weighed (detector-plane) H_3 contributions to the $\psi_{r,r}$ wavefronts, see Eq. (12), at different interferometer unbalance. Left: reference wavefront. Right: measurement wavefront.

To examine the impact of these high-frequency modes, we considered sinusoidal ripples. Hence, the interfering beams are

$$\psi_r(\xi;0) = e^{-\xi^2}\left[1 - i\gamma_r \sin(\omega_r\xi + \beta_r)\right], \tag{29}$$

$$\psi_m(\xi;0) = e^{-\xi^2}\left[1 - i\gamma_m \sin(\omega_m\xi + \beta_m)\right], \tag{30}$$

where $\omega_{r,m}$ and $\beta_{r,m}$ are the angular frequency and phase (relative to the beam axis). The minus $\gamma_{r,m}$ sign makes the signs of $-\gamma\sin(\omega\xi+\beta)$ and $\gamma H_3(\sqrt{2}\xi)$ derivatives (evaluated in $\xi = 0$) equal.

The paraxial propagation of ψ_m in free space is given by the Rayleigh-Sommerfeld propagator. Therefore [19],

$$\psi_m(\xi;\varsigma) = \frac{e^{\frac{i\pi}{4}}\int_{-\infty}^{+\infty} e^{\frac{-i(\xi-\tau)^2}{\varsigma}}\psi_m(\tau;0)\,d\tau}{\sqrt{\pi\zeta}} = \frac{e^{-i\xi^2/q}}{\sqrt{-iq}}\left[1 - i\gamma_m e^{-\frac{(q-i)\omega_m^2}{4q}}\sin\left(\frac{i\omega_m\xi}{q} + \beta_m\right)\right], \tag{31}$$

where $q = i + \varsigma$ and we left out the $\exp(-iks)$ term. Up to the first order of $\gamma_{r,m}$, by using Eq. (29) and Eq. (31) in Eq. (11), we obtain [19]

$$\Delta\phi(\varsigma) = \frac{4}{\pi}\mathrm{Re}\left[F\left(\frac{\sqrt{q}\,\omega_r}{2\sqrt{i+q}}\right)\right]\gamma_r' + 2\mathrm{Im}\left[e^{-\frac{q\omega_m}{4(i+q)}}\mathrm{erf}\left(\frac{\omega_m}{2\sqrt{q}\sqrt{i+q}}\right)\right]\gamma_m', \tag{32}$$

Optics EXPRESS

where $\gamma'_{\mathrm{r,m}} = \gamma_{\mathrm{r,m}} \cos(\beta_{\mathrm{r,m}})$, $F(.)$ is the Dawson's integral [22, Eq. 7.2.5], and erf(.) is the error function. The phase $\beta_{\mathrm{r,m}}$ gauges the ripple impact on $\Delta\phi$; when $\beta_{\mathrm{r,m}} = 0$ is maximum, when $\beta_{\mathrm{r,m}} = \pi/2$ is null.

Figure 5 shows the $\gamma'_{\mathrm{r,m}}$ contributions to $\Delta\phi$ when $\beta_{\mathrm{r,m}} = 0$ rad. The impact depends on the dimensionless frequency $\omega_{\mathrm{r,m}}$; both low and high frequencies make it irrelevant. In the first (long period) case, there is no ripple. In the second (short period) case, the ripple is washed out by integration and propagation. When $\varsigma \approx 0$, the ψ_{m} ripple makes $\Delta\phi$ swing.

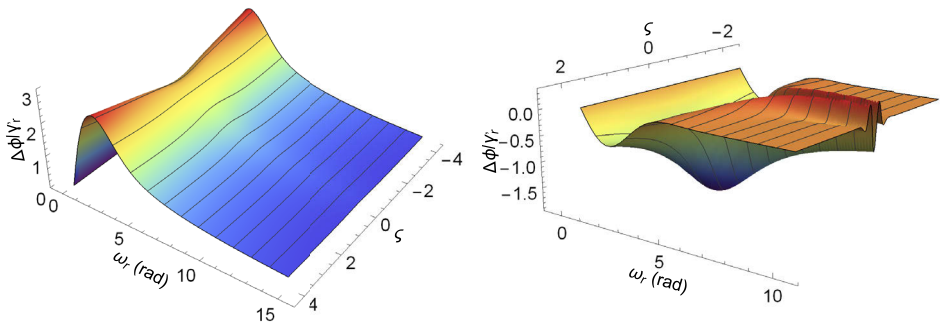

Fig. 5. Ripple contributions – reference (left) and measurement (right) wavefronts – to $\Delta\phi$, see Eq. (32), when $\beta_{\mathrm{r,m}} = 0$ rad.

To check the meaningfulness of Eq. (32), we examine if the near- and far-field limits of Eq. (32) make sense and compare them to the same limits already studied in section 4.2. Figure 6, where we set $\omega_{\mathrm{r,m}} = 2\pi$ rad, shows how the (weighed) wavefront ripples change with the interferometer unbalance – from the $\varsigma = 0$ near-field to the $\varsigma \to \infty$ far-field.

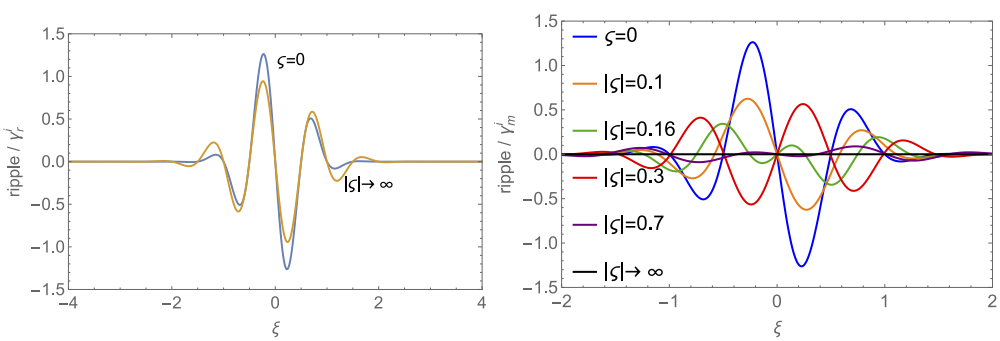

Fig. 6. Weighed (detector-plane) interfering wavefronts, see Eq. (12), at different interferometer unbalance. Left: reference wavefront. Right: measurement wavefront. We set $\omega_{\mathrm{r,m}} = 2\pi$ rad.

As ψ_{m} propagates, the ψ_{r} wavefront-aberration inflates and flattens, but does not change very much. As expected, its contribution to Eq. (32) (see, Fig. 5 left, contour line $\omega_{\mathrm{r}} = 6$ rad) is maximum when $\varsigma = 0$, but almost constant.

Also, the near field offset, consistently with Eq. (27),

$$\lim_{\varsigma \to 0} \Delta\phi = \frac{4F\left(\frac{\omega_{\mathrm{r}}}{2\sqrt{2}}\right)}{\sqrt{\pi}}\gamma'_{\mathrm{r}} - \frac{4F\left(\frac{\omega_{\mathrm{m}}}{2\sqrt{2}}\right)}{\sqrt{\pi}}\gamma'_{\mathrm{m}} \tag{33}$$

is duly proportional to the difference of the wavefront gradients at the beam axes and tends to zero for both low and high frequencies.

Optics EXPRESS

Eventually, Fig. 6 shows that, as $\psi_{\rm m}$ propagates, its wavefront reverses and, eventually, flattens. Consequently, as this figure and Eq. (28) suggest, the far field offset,

$$\lim_{\varsigma\to\pm\infty}\Delta\phi = 2{\rm e}^{-\omega_{\rm r}^2/4}{\rm erfi}(\omega_{\rm r}/2)\gamma'_{\rm r} - \frac{2\omega_{\rm m}{\rm e}^{-\omega_{\rm m}^2/4}}{\sqrt{\pi}\,(1+\varsigma^2)}\gamma'_{\rm m}, \tag{34}$$

where erfi(.) is the imaginary error function and the $\gamma'_{\rm m}$ coefficient vanishes, depends only on $\gamma'_{\rm r}$.

5. Comparison with the experimental data

As shown in Fig. 7, the laser beam is set orthogonal to the analyzer front-mirror by looking at the maximum value of the measured displacement to within 10 μrad uncertainty [12]. The gradient of the wavefront tilt, inferred from the differential signal (green line), is due to the coupling of transverse displacement and curvature of the interfering wavefront. However, when the measured displacement is maximum – that is, when the laser beam is orthogonal and no transverse displacement occurs – the gradient is not null.

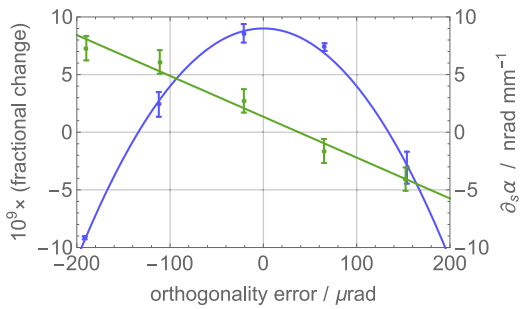

Fig. 7. Blue: fractional changes of the measured displacement of the x-ray/optical interferometer *vs* the deviation δ from a normal incidence of the laser beam on the analyzer front-mirror. Green: gradient of the wavefront tilt inferred from differential sensing when the analyzer is displaced, but driven so as to nullify the pitch rotation. The slope of the best-fit line is $1/R = 0.035$ m^{-1}, the gradient at normal incidence is 1.3 nrad/mm.

The interferometer operated with arms of equal length. The interfering-beam parameters were [23]: wavelength 532 nm; divergence 0.15 mrad, beam-waist radii $w_{0\rm r} = w_{0\rm m} = 1.13$ mm; beam radii at the detection plane $w_{\rm r} = w_{\rm m} = 1.17$ mm; wavefront curvature-radii at the detection plane $R_{\rm r} = R_{\rm m} = R = 28.6$ m; Rayleigh distance $z_{R\rm r} = z_{R\rm m} = 7.53$ m, distance of the detection plane from the beam waists $z_D = 2.14$ m; all estimated to within a 10% uncertainty. The parameters of the TEM$_{00}$ mode in the Eqs. (7) and (8) decompositions are $w_0 = 1.15$ mm and $z_R = 7.82$ m.

If the orthogonality error is equal to δ, a beam propagation by s – which means that the analyzer moves by $s/2$ – shears the interfering beams by $2\xi_0 = s\delta/(\sqrt{2}w_0)$. We differentiated Eq. (23), where $\kappa_{\rm m} + s/z_R$ substitutes for $\kappa_{\rm m}$, to compare the pointing error explaining the 1.3 nrad/mm intercept of Fig. 7 with the 10 μrad uncertainty of the maximum-displacement abscissa. Hence,

$$\partial_s\alpha|_{s/z_R=0} \approx \delta/R, \tag{35}$$

which equation, as shown in Fig. 7, also allowed us determining the wavefront curvature. The $\delta = 37$ μrad pointing error that explains $\partial_s\alpha = 1.3$ nrad/mm is larger that the estimated 10 μrad pointing uncertainty.

Optics EXPRESS

To explain the intercept by a fixed offset $2\xi_0$ between the axes of the interfering beams, we equated and differentiated Eqs. (19) and (25). Hence,

$$\frac{2k\overline{w}}{\sqrt{2\pi}}\partial_s\alpha|_{s=z_D} = \frac{4\sqrt{2}\,\xi_0}{z_R}, \tag{36}$$

where $\partial_s = \partial_\varsigma/z_R$. Since the interfering beams are made collinear to better than 20 μrad and the distance of the detection plane from the interferometer mirrors is less than 1 m, the $0.14w_0 \approx 160$ μm offset explaining the 1.3 nrad/mm gradient is more than the maximum 20 μm expected.

The deviation from flatness of the interferogram – $\lambda/10$ peak-to-peak, see [20,21] – implies that $|\gamma_{\mathrm{r,m}}|$<35 mrad. By equating and differentiating Eqs. (19) and (26), we obtain

$$\frac{2k\overline{w}}{\sqrt{2\pi}}\partial_s\alpha|_{s=z_D} = \partial_s\Delta\phi|_{s=z_D} = (1.09\ \mathrm{m}^{-1})\gamma_{\mathrm{m}}, \tag{37}$$

where the contribution of the reference wavefront is irrelevant. The H_3 contamination explaining $\partial_s\alpha = 1.3$ nrad/mm, $\gamma_{\mathrm{m}} = 13$ mrad, is within the stated maximum.

As regards as the wavefront ripple, by equating and differentiating Eqs. (19) and (32), we obtain

$$\frac{2k\overline{w}}{\sqrt{2\pi}}\partial_s\alpha|_{s=z_D} = \partial_s\Delta\phi|_{s=z_D} = (0.19\ \mathrm{m}^{-1})\gamma'_{\mathrm{m}}, \tag{38}$$

where the contribution of the reference wavefront is irrelevant and we used $\omega_{\mathrm{m}} = 2\pi$, consistently with the observation of a periodicity similar to the radius of the beam spot. The ripple explaining $\partial_s\alpha = 1.3$ nrad/mm is $\gamma'_{\mathrm{m}} = 76$ mrad, a value that is compatible with the observed aberrations. In fact, the $\lambda/10$ interferogram deviation from flatness implies $|\gamma'_{\mathrm{m}}|$<140 mrad, where we used the 0.64 mean of $|\cos(\beta_{\mathrm{m}})|$ over a uniform phase β_{m}.

It is worth noting that a waving wavefront does not propagate along the z axis. Therefore, the propagation direction of ψ_{m} – which is identified by the maximum value of the measured displacement (see Fig. 7) – deviates from the orthogonality by $\delta_0 = p_0/(kw_0)$, where

$$p_0 = \gamma_{\mathrm{m}}\omega_{\mathrm{m}}\mathrm{e}^{-\omega_{\mathrm{m}}^2/8}\cos(\beta_{\mathrm{m}}) \tag{39}$$

is the (dimensionless and first order) center-of-mass of the power spectrum of the wave-vector transverse-components. By using $\omega_{\mathrm{m}} = 2\pi$ and $\gamma_{\mathrm{m}}\cos(\beta_{\mathrm{m}})$<140 mrad, we obtain δ_0<0.7 μrad. Therefore, the off-axis propagation is irrelevant.

6. Conclusion

We realized an optical interferometer which uses a single laser beam to measure displacements and tilts of an x-ray interferometer simultaneously and with picometer and nanoradian resolutions. It applies differential wavefront sensing to decouple and measure three degrees of freedom via the local phases of the interference pattern inferred by the signals of a quadrant photodiode. We noted that the optical and x-ray measurements of the parasitic pitch-rotation associated to the displacement of the movable crystal disagree. In this paper, we developed an analytical model of the interferometer operation and investigated how the tilt-free propagation of mismatched and aberrated wavefronts, otherwise parallel, affects the differential phase.

We proved that mismatches and aberrations couple to the propagation and explain the disagreement observed. The false inference of tilted beams is due to the offset of the differential-phase readout. It originates from the offset between the beam axes and the contaminations by the TEM_{30} mode. Furthermore, since the readout offset depends on the propagation distance, we also infer a (non-existent) parasitic tilt associated with the propagation of the measurement beam.

This result strengthens the confidence in the measurement of the silicon lattice parameter, which was essential to determine the Avogadro and Planck constants and will be still necessary

Optics EXPRESS

to realize the kilogram following the redefinition of the International System of Units based on defining constants. Our formalism may also help to investigate the operation the LISA interferometer when measuring the tilt of the received wavefront and test mass.

Disclosures

The authors declare that there are no conflicts of interest related to this article.

References

1. A. Bergamin, G. Cavagnero, and G. Mana, "A displacement and angle interferometer with subatomic resolution," Rev. Sci. Instrum. **64**(11), 3076–3081 (1993).
2. E. Morrison, B. J. Meers, D. I. Robertson, and H. Ward, "Automatic alignment of optical interferometers," Appl. Opt. **33**(22), 5041–5049 (1994).
3. T. Schuldt, M. Gohlke, D. Weise, U. Johann, A. Peters, and C. Braxmaier, "Picometer and nanoradian optical heterodyne interferometry for translation and tilt metrology of the LISA gravitational reference sensor," Classical Quantum Gravity **26**(8), 085008 (2009).
4. S. R. Gillmer, R. C. G. Smith, S. C. Woody, and J. D. Ellis, "Compact fiber-coupled three degree-of-freedom displacement interferometry for nanopositioning stage calibration," Meas. Sci. Technol. **25**(7), 075205 (2014).
5. G. Wanner, G. Heinzel, E. Kochkina, C. Mahrdt, B. S. Sheard, S. Schuster, and K. Danzmann, "Methods for simulating the readout of lengths and angles in laser interferometers with gaussian beams," Opt. Commun. **285**(24), 4831–4839 (2012).
6. X. Yu, S. R. Gillmer, and J. D. Ellis, "Beam geometry, alignment, and wavefront aberration effects on interferometric differential wavefront sensing," Meas. Sci. Technol. **26**(12), 125203 (2015).
7. H.-Z. Duan, Y.-R. Liang, and H.-C. Yeh, "Analysis of non-linearity in differential wavefront sensing technique," Opt. Lett. **41**(5), 914–917 (2016).
8. G. Heinzel, A. Rüdiger, R. Schilling, K. Strain, W. Winkler, J. Mizuno, and K. Danzmann, "Automatic beam alignment in the Garching 30-m prototype of a laser-interferometric gravitational wave detector," Opt. Commun. **160**(4-6), 321–334 (1999).
9. H. Grote, G. Heinzel, A. Freise, S. Goßler, B. Willke, H. Lück, H. Ward, M. M. Casey, K. A. Strain, D. I. Robertson, J. Hough, and K. Danzmann, "Alignment control of GEO 600," Classical Quantum Gravity **21**(5), S441–S449 (2004).
10. F. Acernese, M. Alshourbagy, F. Antonucci, S. Aoudia, K. Arun, P. Astone, G. Ballardin, F. Barone, M. Barsuglia, T. Bauer, S. Bigotta, S. Birindelli, M. Bizouard, C. Boccara, F. Bondu, L. Bonelli, L. Bosi, S. Braccini, C. Bradaschia, A. Brillet, V. Brisson, H. Bulten, D. Buskulic, G. Cagnoli, E. Calloni, E. Campagna, B. Canuel, F. Carbognani, L. Carbone, F. Cavalier, R. Cavalieri, G. Cella, E. Cesarini, E. Chassande-Mottin, S. Chatterji, F. Cleva, E. Coccia, J. Colas, M. Colombini, C. Corda, A. Corsi, J.-P. Coulon, E. Cuoco, S. D'Antonio, A. Dari, V. Dattilo, M. Davier, R. D. Rosa, M. D. Prete, L. D. Fiore, A. D. Lieto, M. D. P. Emilio, A. D. Virgilio, V. Fafone, I. Ferrante, F. Fidecaro, I. Fiori, R. Flaminio, J.-D. Fournier, S. Frasca, F. Frasconi, L. Gammaitoni, F. Garufi, E. Genin, A. Gennai, A. Giazotto, M. Granata, V. Granata, C. Greverie, G. Guidi, H. Heitmann, P. Hello, S. Hild, D. Huet, P. L. Penna, M. Laval, N. Leroy, N. Letendre, M. Lorenzini, V. Loriette, G. Losurdo, J.-M. Mackowski, E. Majorana, C. Man, M. Mantovani, F. Marchesoni, F. Marion, J. Marque, F. Martelli, A. Masserot, F. Menzinger, C. Michel, L. Milano, Y. Minenkov, M. Mohan, J. Moreau, N. Morgado, S. Mosca, B. Mours, I. Neri, F. Nocera, G. Pagliaroli, C. Palomba, F. Paoletti, S. Pardi, A. Pasqualetti, R. Passaquieti, D. Passuello, G. Persichetti, F. Piergiovanni, L. Pinard, R. Poggiani, M. Punturo, P. Puppo, O. Rabaste, P. Rapagnani, T. Regimbau, F. Ricci, A. Rocchi, L. Rolland, R. Romano, P. Ruggi, B. Sassolas, D. Sentenac, B. Swinkels, R. Terenzi, A. Toncelli, M. Tonelli, E. Tournefier, F. Travasso, J. Trummer, G. Vajente, J. van den Brand, S. van der Putten, D. Verkindt, F. Vetrano, A. Viceré, J.-Y. Vinet, H. Vocca, M. Was, and M. Yvert, "Automatic alignment for the first science run of the Virgo interferometer," Astropart. Phys. **33**(3), 131–139 (2010).
11. D. Schuetze, "Measuring earth: Current status of the GRACE follow-on laser ranging interferometer," J. Phys.: Conf. Ser. **716**, 012005 (2016).
12. E. Massa, C. P. Sasso, G. Mana, and C. Palmisano, "A more accurate measurement of the 28Si lattice parameter," J. Phys. Chem. Ref. Data **44**(3), 031208 (2015).
13. A. Bergamin, G. Cavagnero, and G. Mana, "Observation of Fresnel diffraction in a two-beam laser interferometer," Phys. Rev. A **49**(3), 2167–2173 (1994).
14. G. Basile, A. Bergamin, G. Cavagnero, and G. Mana, "Phase modulation in high-resolution optical interferometry," Metrologia **28**(6), 455–461 (1991).
15. A. Bergamin, G. Cavagnero, and G. Mana, "Accuracy assessment of a least-squares estimator for scanning x-ray interferometry," Meas. Sci. Technol. **2**(8), 725–734 (1991).
16. U. Levy, S. Derevyanko, and Y. Silberberg, "Light modes of free space," in *Progress in Optics*, vol. 61 T. D. Visser, ed. (Elsevier, 2016), pp. 237–281.
17. A. E. Siegman, *Lasers* (University Science Books, 1986).
18. G. Mana and C. P. Sasso, "Corrections of the travelling-fringe period for the interference of aberrated beams," Metrologia **56**(5), 055004 (2019).
19. Wolfram Research, Inc., "Mathematica, Version 11.1," (2017). Champaign, IL.

Optics EXPRESS

20. A. Balsamo, G. Cavagnero, G. Mana, and E. Massa, "Retrieval of the phase profile of digitized interferograms," J. Opt. A: Pure Appl. Opt. **5**(4), 418–424 (2003).
21. C. P. Sasso, E. Massa, and G. Mana, "Diffraction effects in length measurements by laser interferometry," Opt. Express **24**(6), 6522–6531 (2016).
22. "*NIST Digital Library of Mathematical Functions*," http://dlmf.nist.gov/, Release 1.0.22 of 2019-03-15. F. W. J. Olver, A. B. Olde Daalhuis, D. W. Lozier, B. I. Schneider, R. F. Boisvert, C. W. Clark, B. R. Miller and B. V. Saunders, eds.
23. G. Mana, E. Massa, C. P. Sasso, B. Andreas, and U. Kuetgens, "A new analysis for diffraction correction in optical interferometry," Metrologia **54**(4), 559–565 (2017).